Unraveling the surface formation of regular and deuterated water in space : a combined laboratory and computational study

Lamberts, A.L.M.

2

METHODS: EXPERIMENTAL SOLID-STATE ASTROCHEMISTRY

The knowledge on gas-phase reactions occuring in interstellar clouds cannot be extrapolated as to describe the same reaction taking place on the surface of a dust grain. In the solid state not only more intermolecular interactions can play a role, such as the influence of the neighboring molecules, but reactions are also in competition with the other processes that can take place simultaneously. A study devoted to astrochemically relevant surface reactions is therefore crucial in understanding the key proceses at play for, *e.g.*, water formation and detection in the interstellar medium. In this Thesis we will use precisely such dedicated experiments conducted in an ultra-high vacuum setup equipped with reflection absorption infrared spectroscopy and a quadrupole mass spectrometer. These two analytical techniques are complementary: infrared spectroscopy can be performed in situ, whereas the mass can be detected only if ices are sublimated.

This chapter starts with an overview of the relevant surface science techniques applied in experimental astrochemistry, putting the system and procedures employed in Chapters 6-8 in perspective. Secondly, a detailed description of the used setup, SURFRESIDE^2, is documented.

Based on S. Ioppolo, G. Fedoseev, T. Lamberts, C. Romanzin and H. Linnartz, *SURFRESIDE^2: An Ultrahigh Vacuum System for the Investigation of Surface Reaction Routes of Interstellar Interest*, Rev. Sci. Instrum. 84 (2013) 073112

2.1 INTRODUCTION

The dust grains present in the interstellar medium (ISM) play an important role in the synthesis of saturated species as explained in the Introduction. On average in a relatively cold and dense interstellar region ($n_H = 10^4$ cm^{-3}, 10 K) maximum one hydrogen atom arrives on the grain surface per day (Tielens, 2013) and mimicking such reactions in the laboratory inherently means changing the timescale at which they take place. In other words, reactions on the experimental surface occur rapidly one after the other, or simultaneously. Note that the main assumption made is therefore that thermalization on the surface and in the ice is fast enough to ensure that excess reaction heat cannot be used to overcome reaction barriers. Since many reactions can occur at the same time it is crucial to make use of a bottom-up approach: constructing a reaction network from single well-understood processes. A first step in this direction is to use surface science techniques at cryogenic temperatures to recreate conditions as similar as possible to those in the ISM. The first experiments designed specifically to probe atom-addition reactions against an astrochemical background were performed by Hiraoka et al. (1994) and revolved around the hydrogenation of CO at $10 - 20$ K. In the past decades the number of experimental studies devoted to astrochemistry has increased tremendously.

In general, an experimental setup consists of five parts: (i) a main chamber, (ii) a substrate, (iii) deposition lines, (iv) ice processing techniques, and (v) analytical tools. A division can be made between main chambers under high vacuum (HV, $10^{-5} - 10^{-7}$ mbar at room temperature) and ultra high vacuum (UHV, $10^{-8} - 10^{-11}$ mbar at room temperature). Note that originally all experiments were performed in HV setups, which resulted in the investigation of ices with thicknesses up to several μm. A big disadvantage of the relatively high pressures in the chamber is the continuous deposition of the largest contaminant: water. This can be minimized by reducing the pressure and baking the system, *i.e.*, working under UHV. Another advantage is the possibility to work with thin film ices or even perform sub-monolayer studies. A monolayer corresponds to $0.5 - 1 \times 10^{15}$ molecules cm^{-2}, depending on the species at hand. The deposition lines are typically held under vacuum when they are not used to reduce the number of possible contaminants entering the main chamber. The substrates used, ice processing techniques, and the analytical tools will be reviewed below.

This chapter first focuses on experimental techniques used in astrochemistry in general and then discusses the setup used for this Thesis, SURFRESIDE^2, in particular.

2.2 DEPOSITION AND PROCESSING OF ICES

2.2.1 *Surfaces*

The substrate surfaces used in an experimental setup can be aimed either at reproducing the characteristics of interstellar dust grains or at being advantageous for one particular experimental technique.

Imitating an interstellar surface serves in particular the studies focusing on the surface-molecule interaction and its influence on the reactions at hand, *i.e.*, monolayer and submonolayer studies. Interstellar dust grains are thought to be of carbonaceous and/or silicaceous origin (Hony, 2003; Gibb et al., 2000) and therefore these types of surfaces have been implemented in experimental setups. Highly ordered pyrolytic graphite (HOPG) has been used as a carbonaceous grain analog (Brown et al., 2006; Thrower et al., 2011; Minissale et al., 2014). Amorphous silicate substrates, $(SiO)_x$, have also been employed and the influence of various

structures with respect to H_2 formation has been characterized (Dulieu et al., 2013; Abdulgalil et al., 2013; Sabri et al., 2014).

Substrates made from certain metals can be used intentionally to avoid any interaction between the ice and the surface, such as Au (used as a substrate throughout the work described in this Thesis), Al (Oba et al., 2010), or Cu (Gavilan et al., 2012). An advantage of these substrates is that they are highly reflective, which is exploited by reflection absorption infrared experiments (see Section 2.3.1). However, it can also be desirable to have a substrate that is transparent to infrared radiation, such as CsI, KBr, ZnSe, and Si if spectra are acquired in an infrared transmission mode (Öberg et al., 2009; Palumbo et al., 2010; Islam et al., 2014).

Finally, to ensure the separation between the ice studied and the surface or to study the influence of a particular ice on reaction mechanisms (*e.g.*, polar vs. non-polar ice) an intermediate layer of ice can be deposited on the substrate prior to the experiment.

2.2.2 *Ice deposition*

When ices are deposited at low temperatures, this can be thought of to occur via a ballistic hit-and-stick mechanism, because there is not enough thermal energy available per species to scan the surface and find the most favourable position. This implies that the morphology depends on the angular distribution of the water molecules incident from the gas phase (Stevenson et al., 1999). For water ice, perpendicular deposition results in the lowest porosity, which increases by using more glancing angles. Background deposition, probably most similar to interstellar conditions, leads to the highest porosity. The main disadvantage there is, however, that the main chamber is fully filled with the depositing species.

In general, two types of deposition experiments can be performed: sequential deposition and co-deposition. In the case of sequential deposition, one of the reactants is first deposited on the sample and subsequently exposed to the second reactant (typically a thermal atom-beam, see Section 2.2.3.2). The formation and destruction of intermediates then leads to the creation of final, stable products. Plotting surface abundances versus time allows for the derivation of reaction rates of these products. However, the yields are often limited due to the low penetration depth of the atoms into the ice layer. Moreover, the reactivity of the intermediate species (often radicals) does not allow for their unambiguous identification. During co-deposition, on the contrary, all reactants enter the experimental setup simultaneously. The ratio between them can be varied and in this way either a high yield of final products can be obtained or the formation of intermediate species can be probed. These two types of deposition techniques are complementary.

If ices are thick enough, the laser interference pattern of a He-Ne laser being reflected by both the vacuum-film and the film-substrate interfaces can be used to monitor the thickness of the ice film during ice deposition (*e.g.*, Palumbo et al. (2010)).

2.2.3 *Ice processing*

2.2.3.1 *Thermal processing*

Increasing the temperature of the substrate mimics the evolution of a dark cloud collapsing and leads to the formation of a protostar that heats up its surroundings. The main effects of thermal processing are diffusion, segregation, crystallization, and sublimation. Elevated temperatures are also thought to activate chemistry (Duvernay et al., 2010).

Diffusion increases with increasing temperature because there is more energy available thermally for species to overcome the binding energy to its neighbors. For instance CO diffu-

sion through a H_2O layer can be probed at different temperatures with infrared spectroscopy (Mispelaer et al., 2013; Karssemeijer et al., 2014). Diffusion can ultimately lead to the collapse of originally porous ices (Bossa et al., 2012).

Segregation can occur in mixed ices if the mutual binding energy between two different species is less than the binding energies of those species with themselves. A prominent example in astrochemistry is the segregation of CO_2 and H_2O in originally mixed ices, driven by the strong (hydrogen bonded) interaction between water molecules (Ehrenfreund et al., 1998; Öberg et al., 2009).

The amorphous ices deposited at low temperature can crystallize when given enough time or energetic input. In the case of water, for instance, slow deposition at 10 K results in an amorphous solid. Increasing the temperature to 130 K results first in irreversible annealing of the ice followed by a transformation into polycrystalline cubic ice. At temperatures higher than 150 K the hexagonal structure can be found (Fletcher, 1971; Hagen et al., 1983).

Finally, if temperatures rise high enough, the binding energy to the surface can be overcome and species are sublimated into the gas phase where it can be detected by, *e.g.*, a mass spectrometer.

2.2.3.2 *Atom addition experiments*

The most obvious origin of chemistry taking place on surfaces is by bringing one or more reactive components together. Typical reactive species are radicals and these can be generated in several ways described below.

Thermal cracking is a common practice to generate H (D) atoms from a H_2 (D_2) beam that passes through a tungsten heated hot ($\sim$ 2000 K) capillary (Tschersich & von Bonin, 1998; Tschersich, 2000; Tschersich et al., 2008). Such commercially available systems have been widely used in laboratory astrochemistry (Baouche et al., 2006; Ioppolo et al., 2008; Minissale et al., 2014). In a similar way, oxygen atoms can also be generated, but such thermal cracking beamlines are designed to be used for a single species, either hydrogen (deuterium) or oxygen. For other species the temperatures required for breaking a bond are too high.

A microwave discharge plasma, on the contrary, can be used to generate a range of radicals by cracking molecules in the plasma. In principle a plasma can break the bonds of H_2, D_2, O_2, N_2, H_2O, NH_3, etc, yielding their respective radical fragments. The ions that are simultaneously generated can be deflected after leaving the plasma chamber to assure that they do not reach the sample surface. Such a source is typically operated at 2.45 GHz and is both commercially available, making use of the electron cyclotron resonance effect (Anton et al., 2000), but can also be made in-house (McCullough et al., 1993; Timmermans et al., 1998). Both types of sources have been reported in astrochemical literature (Oba et al., 2010; Minissale et al., 2014).

Alternatively, a radio-frequency generated plasma operating in the MHz regime can also be used (Sibener et al., 1980; Pirronello et al., 1997; He et al., 2014).

Both feedgas molecules and product fragments can be excited, some in (metastable) long lived states. To ensure that this excitation energy is not transferred to the ice, changing the structure, or is used to overcome reaction barriers, such species need to be quenched. This is setup dependent, one example is described in Section 2.4.4.

In order to be able to extrapolate experimental results to interstellar timescales, it is crucial to quantify the atom fluxes and dissociation efficiencies carefully. There is a wide range of possibilities available to do so and here we only summarize several that have been used in the astrochemical community. Quantification of a hydrogen atom beam can be performed by using a quadrupole mass spectrometer (QMS, see below) and comparing masses 1 and 2 with the (microwave) source switched on and off (Hidaka et al., 2004). Nagaoka et al. (2007) used

a time-of-flight setup equipped with a QMS to determine the translational temperature of a cooled atomic hydrogen (deuterium) beam. The presence of OH in a microwave plasma of H_2O has been proven with the use of Resonance Enhanced Multiphoton Ionization (REMPI). Finally, in Section 2.4, we will discuss the reference reaction technique to derive O- and N-atom fluxes based on measuring the yield of products of a barrierless reaction.

2.2.3.3 *Energetic processing*

Interstellar ices can also be subject to particles of a more energetic nature, which is the case for ices that interact with cosmic rays. While cosmic rays are composed primarily of high-energy nuclei, interactions with molecules can result in secondary electrons and photons being generated as well. The energies involved for these three types of irradiation is quite different: UV photons lie in the range of 7-14 eV, electrons around keV and cosmic rays can be mimicked experimentally up to MeV.

In general, the effects of energetic processing are sputtering (or desorption), structural changes, chemistry, (ion) implantation, and residue formation on the substrate. To discuss all of these effects falls outside the scope of this Thesis, but some recent developments in vacuum ultraviolet (VUV) irradiation, ion and electron bombardment experiments will be discussed below.

VUV irradiation of interstellar ice analogs is commonly brought about by so-called microwave discharge hydrogen-flow lamps and have already been used in the early days of laboratory astrochemistry (Hagen et al., 1979). They produce atomic hydrogen Ly-α (121.6 nm) and hydrogen molecular emission in the 110-180 nm regime. Despite its widespread use, the characterization of these lamps in terms of H_2 pressure, lamp geometry, and seed gas is a recent development (Chen et al., 2014).

Studies focusing on the influence of VUV on the chemistry show that irradiating mixed interstellar ice analogs is powerful enough to lead to the formation of complex molecules (Bernstein et al., 2002; Muñoz Caro et al., 2002). A more quantitative investigation of the separate reaction routes is needed in order for the results of laboratory work to be implemented in astrochemical models and new experimental setups aiming to do so have indeed been reported (Paardekooper et al., 2014). Besides inducing chemistry, VUV irradiation can also result in the photodesorption of the top layers of the ice. The desorption efficiency is in fact wavelength dependent which can be probed at the SOLEIL synchrotron facility (Fayolle et al., 2011; Bertin et al., 2012).

Ions can be generated with an ECR ion source, an ion accelerator with a magnetic mass filter or with a commercially available ion source (Sivaraman et al., 2013; Bennett et al., 2014; Raut et al., 2012). Ion irradiation experiments can be performed in three ways: ions passing through the ice-covered sample, irradiation during ice deposition, and ion implantation. The thicker the ice involved, the more ions can be implanted. Many ionization studies (both using ions and electrons) are performed in the light of their relevance to the outer solar system (Raut et al., 2012; Raut & Baragiola, 2013). Although numerous investigations have been performed, again, the quantification of such setups is crucial and to that end, new setups have lately been constructed (Jones & Kaiser, 2013).

A direct comparison between the effects of ion irratiation and UV photolysis, in terms of dose (eV per mass unit), is available for many systems, *e.g.*, CH_4, CH_3OH, and CO (Baratta et al., 2002; Loeffler et al., 2005).

2.3 ANALYTICAL TECHNIQUES

2.3.1 *Infrared spectroscopy*

Surface science traditionally does not particularly make use of vibrational, infrared (IR) spectroscopy as an analytical technique. Astronomy, however, does. Rotational spectroscopy would in fact be preferable, because those states can be thermally excited and can therefore be probed in emission. In the solid state, however, rotation is quenched. Electronic transitions, or UV-Vis radiation, are not typically used, because the energy is too high and destroys both the ice structure as well as the molecules (see Section 2.2.3.3).

Remember that vibrations can be excited only if the transition moment is non-zero, which occurs mainly for molecules with a non-zero electric dipole moment, *i.e.*, a molecule such as O_2 does not absorb IR radiation, whereas H_2O does. The fundamental transitions – those occuring if one quanta of energy is absorbed – correspond to the strongest detected signals. Overtones, where multiple quanta are absorbed, or combination bands, when more than one normal mode is involved, are less intense. The types of vibrations that can occur are for instance symmetrical and antisymmetrical stretching, bending, torsion, and umbrella modes. Molecules that are not infrared active can still be observed in the ISM through quadrupolar and magnetic dipolar transitions. Finally, electronic emission spectroscopy can also be employed.

Here, we highlight two possible experimental types of operation: transmission and reflection as depicted in Fig. 2.1. From the figure it is apparent that in transmission thicker ices are required (HV conditions), while the thin films grown under UHV conditions can only be analyzed if the pathlength is increased via a reflection of the beam on the surface. Changing the angle of incidence also has an effect on the absorption frequency detected. The long-range dipole-dipole coupling can manifest itself in a frequency difference (several cm^{-1}) between the longitudinal and the transverse optical modes. This is a result of the long range electric fields associated with long-wave longitudinal phonons. TO phonon vibrations are characterised by atomic displacements perpendicular to the wavevector whereas for LO vibrations, the atomic displacements are parallel to the wavevector. In transmission at normal incidence, only the TO mode is active, but both modes are active at oblique incidence. In reflection spectroscopy on a metal surface, only the LO mode band is observed, due to the electric field in the metal. See Palumbo et al. (2006) for an in-depth discussion of the LO-TO splitting of the fundamental CO band at 2140 cm^{-1}. Note that originally, all astrochemical experiments were performed in a HV setup and hence made use of transmission infrared spectroscopy (*e.g.*, Sandford & Allamandola (1988); Palumbo & Strazzulla (1993); Ehrenfreund et al. (1997)).

A typical experiment consists of recording absorption spectra at selected time intervals with respect to an initially recorded background spectrum. This background spectrum corrects for the gas-phase absorption that the infrared beam encounters on its way from the source through the vacuum chamber to the detector.

Given a spectrum, both experimentally and observationally, a quantitative analysis in terms of a number of absorbing molecules is needed. This is achieved by integrating a selected infrared absorption band to obtain the band area and subsequently divide this by the so-called band strength. The band strength is a value for the number of molecules corresponding to a fixed amount of absorption. Although these band strengths are readily available for spectra recorded in transmission mode, they depend on the substrate and structure of the sample (Gerakines et al., 1995; Fulvio et al., 2009). Moreover, in the reflection mode, they are highly setup-dependent (see Section 2.4.3).

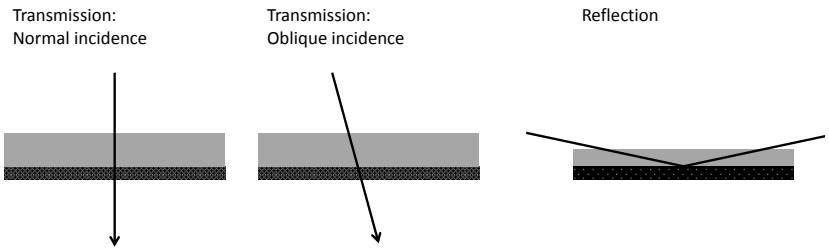

Figure 2.1: Two types of infrared spectroscopy if ice films: transmission and reflection.

Although IR spectroscopy has proven to be of great use in astrochemistry, there are certainly drawbacks. First, mainly particular functional groups are detected, such as -CH or -OH moieties, instead of molecules themselves. Therefore, if the functional group strongly interacts with its surrounding the absorption band is broadened and can easily overlap with that of another molecule. This becomes especially troublesome when dealing with large, but non-abundant species of which the signal would be buried within that of more abundant species. Furthermore, transitions at IR frequencies correspond to intramolecular vibrational modes of the molecules in the ice, and therefore, detects only local changes in structure. TeraHertz (THz) or far-IR spectroscopy, actually probes the lower frequency vibrations that correspond to low energy intra- and, especially, intermolecular modes and as such is sensitive to large-scale structural changes. This also means that, in principle, astronomical THz observations can be obtained in the absence of a background radiation source (Allodi et al., 2014).

Finally, the sensitivity or IR spectroscopy is rather low, even if reflection absorption spectroscopy is used: a minimum of ~ 0.5 ML is needed for a signal to be clearly detected (see for instance Chapter 6). Mass spectroscopy, on the other hand, has a much lower detection limit and as such is more suitable for submonolayer studies (Noble et al., 2011).

2.3.2 *Temperature Programmed Desorption*

Complementary to in situ IR spectroscopy, Temperature Programmed Desorption (TPD) experiments can be performed during which ice sublimation is probed. TPD experiments are usually performed in an UHV set-up equipped with a quadrupole mass spectrometer (see below), but can also be used in conjuction with, *e.g.*, Resonance Enhanced Multiphoton Ionization and Time of Flight spectrometry (REMPI-TOF) (Gavilan et al., 2012).

The experiment consists of two phases: first, the substrate is kept at a constant low temperature and a known quantity of one or multiple species is deposited; during the second phase the temperature is linearly increased and the desorption of surface species is monitored using the mass spectrometer. The measured desorption rate of the species is then plotted as a function of temperature.

In this way, species produced on the surface and in the ice can be detected, usually according to their masses. Knowing the desorption temperature, the corresponding emerging mass and simultaneous disappearing infrared feature often provides enough handles to determine a reaction product.

More quantitative studies can also be performed, aiming to derive a binding energy. One can perform a series of TPD experiments, varying the initial deposited amount, the deposition

temperature, and/or the heating ramp. Often, the resulting TPD spectra are then fitted by the Polanyi-Wigner equation

$$\frac{d}{dT} n_g(A) = n_s(A)^o \frac{\nu \exp(-E_{bind,A}/k_B T)}{\beta} \quad (2)$$

where o is the order of the desorption process and β is the heating rate. Generally the order is assumed and the prefactor, ν, and binding energy, $E_{bind,A}$, are used as fitting parameters. Unfortunately, these two parameters are correlated and it is not straightforward to get accurate values for both parameters simultaneously. Therefore, sometimes the prefactor is assumed as well and only the binding energy is obtained from the fit.

Zeroth order desorption generally occurs when multiple layers of the same species are deposited. During the desorption, the number of surface species available for desorption (the top layer) remains the same. For first order desorption, the temperature for which the desorption rate peaks is independent of the deposited amount. First order desorption generally occurs in the monolayer regime, where all surface species are also available for desorption. Finally, second order desorption is mainly due to two reasons: either desorption of reaction products, that were formed in a second order surface reaction, or the surface exhibits a distribution of binding sites. In the latter case, the stronger binding sites are filled first and the average binding energy decreases with coverage, resulting in TPD curves that resemble second order behavior.

Care has to be taken in concluding which chemistry occurs at low temperature on the surface and during the warm-up phase. Typically, this is done through a variety of control experiments. For instance, an experiment can be performed at different temperatures followed by TPD. If the Langmuir-Hinshelwood mechanism is responsible for a reaction, the results of the TPD should differ. If no difference is found, the spectrum obtained might well be caused by secondary reactions.

The binding energies of a wide collection of stable species have been determined using the TPD technique. Examples are N_2 (Öberg et al., 2005), CO (Öberg et al., 2005), O_2 (Acharyya et al., 2007), H_2O (Bolina et al., 2005; Fraser et al., 2001), and CH_3OH (Green et al., 2009). The binding energies have been mostly determined for the desorption of pure ices from different substrates. Since interstellar ices are not homogeneous the desorption of mixed layers is more relevant for astrochemical modeling. However, the introduction of more species in the ice makes the desorption process immediately much more complex. First, the binding energy of a particle can change depending on its surrounding material. Second, the dominant mantle species can prevent other species from desorbing.

2.3.3 *Mass spectrometry*

As mentioned in the previous section, mass spectrometry is often used in conjunction with a TPD experiment. Its working principle makes use of the interaction of a magnetic and/or electric field with the mass-to-charge ratio of a charged particle. Ionizing a species can be achieved with electrons generated by a hot filament or through single photon ionization (see Section 2.4 and Kaiser et al. (2014)).

A circular path is brought about by a magnetic (Lorentz) force that acts on a moving charged particle. This force depends on the velocity and can be couteracted by an electric force (in the presence of an electric field). Therefore, if the electric and magnetic forces are in equilibrium, only particles with a matching velocity are selected, which in turn depends on the mass-to-charge, m/z, ratio. It is precisely the latter characteristic that can be detected by varying the magnetic field.

In practice it is not straightforward to achieve stable and spatially uniform magnetic fields with permanent magnets. Instead, a quadrupolar electric field can be implemented with the use of four metal rods where two opposing rods have an applied potential negative with respect to that of the remaining two rods. All rods have both an alternating and direct current (AC and DC) potential. The DC components act as a mass filter: the positive component destabilizes low masses, whereas the negative component does the same for high masses. The alternating current allows ions of the right m/z ratio to travel in an oscillatory motion through the rods until the detector is reached. Again, the influence of the electric fields depends on the mass and charge of the species and by tuning the voltages the double mass filter only allows a narrow range of mass-to-charge ratios to pass through the quadrupole. By scanning the voltages, a mass spectrum is generated.

Although a narrow range of m/z ratios can be selected, the uncertainty is typically of the order of 1 amu, *i.e.*, for instance the molecules CO and N_2 cannot be distinguished. An alternative is provided by a time-of-flight (TOF) mass spectrometer. In that case, the generated ions are extracted by a potential into the flight tube where the long pathlength separates the species according to their velocity. The potential energy given to the ions during the extraction depends on the charge and is converted into kinetic energy given its mass, hence again the m/z ratio determines the velocity and therefore the time of arrival at the detector. To increase the pathlength a reflectron can be placed at the end of the tube, reflecting the ions in the direction of the second detector. This increases the separation between the detection of different ions, *i.e.*, the mass resolution.

Possible detectors include secondary electron multipliers, microchannel plate detectors, Daly detectors, and Faraday cups (see Section 2.4.2).

2.3.4 *Other analytical techniques*

To study the effects of sputtering, *i.e.*, acquire knowledge about the mass removed from a target given a particular ion fluence, a quartz-crystal microbalance (QCM) is very useful. Coupling such a QCM to a mass spectrometer allows to distinguish the molecular species emitted from the targets as well (Loeffler & Baragiola, 2010; Raut & Baragiola, 2011).

A clear disadvantage of TPD experiments is the destruction of the ice that is under investigation and the fact that thermal chemistry could be induced. Another approach is to ablate a fraction of the ice, for instance via Matrix-Assisted Laser Desorption/Ionization (MALDI). The resulting plume of molecules can then be analyszed and if a TOF mass spectrometer is coupled to such a setup it is possible to work with large molecules or complex mixtures (Gudipati & Yang, 2012; Paardekooper et al., 2014). REMPI can provide valuable information concerning excited states of species formed on the surface (Watanabe et al., 2010; Gavilan et al., 2012).

2.4 SURFRESIDE^2 - SYSTEM DESCRIPTION

The focus of this section is on a quantitative characterization of the experimental properties of the setup used throughout this thesis: the SURFace REaction SImulation DEvice - 2 or SURFRESIDE^2. A new approach to fully characterize atom fluxes has been used and is outlined below. SURFRESIDE^2 consists of three distinct UHV chambers (Fig. 2.2). In the main chamber, ices are deposited with monolayer precision and processed at astronomically relevant temperatures. Reflection Absorption Infrared (RAIR) spectroscopy and Temperature Programmed Desorption (TPD) are used as analytical tools to characterize the ice composition. In the other chambers different atom sources are mounted for the controlled production of

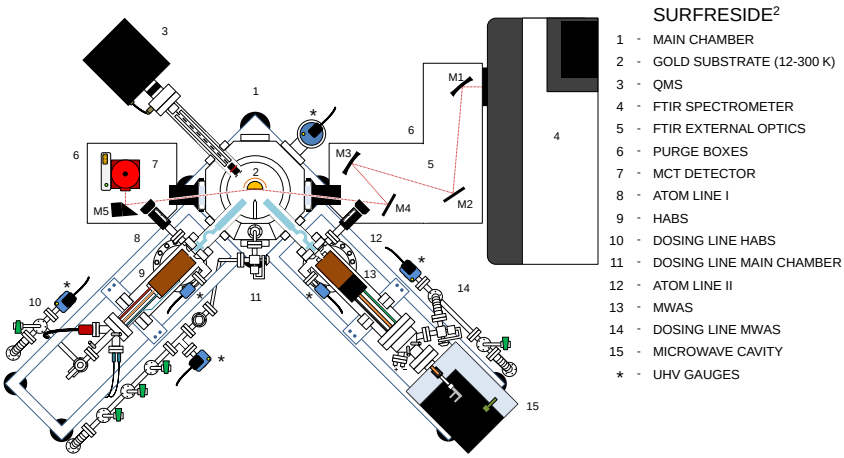

Figure 2.2: A schematic top-view of the experimental apparatus.

well-characterized atom (molecular) beams. Shutters separate the beam line chambers from the main chamber and allow an independent operation of the individual beam lines.

2.4.1 *Main Chamber*

The custom-made ultrahigh vacuum 304 stainless steel main chamber has a diameter of 30 cm and is provided with eight lateral CF 35, two lateral CF 16, one top CF 63 and one bottom CF 200 flange connections (#1 in Fig. 2.2). A gate valve connects the bottom-flange with a 260 l/s (for N_2) turbomolecular pump (Pfeiffer Vacuum, TMU 261P). The CF 35 lateral flanges are used to connect the main chamber to the two atom lines (#8 and #12 in Fig. 2.2), an active cold cathode transmitter (Pfeiffer Vacuum, IKR270) for pressure readings in the $5 \cdot 10^{-11}$ - 0.01 mbar range, and a quadrupole mass spectrometer (QMS; Spectra - Microvision Plus; #3 in Fig. 2.2). Two CF 35 windows are used for in- and out-going light from a Fourier transform infrared spectrometer (FTIR; Agilent Technologies Cary 600 Series; #4 in Fig. 2.2). The two CF 16 flanges are used as inlet for a double ice deposition dosing line (#11 in Fig. 2.2), while a differentially-pumped (Leybold Vacuum, TW 300) ϑ rotatable stage (0°-360°) connects the top-flange to a helium closed-cycle refrigerator (ASR Inc.; #2 in Fig. 2.2).

The room temperature base pressure of the main chamber is in the low 10^{-10} mbar regime. An optically-flat gold-coated copper substrate ($2.5 \cdot 2.5$ cm^2) is placed in the center of the main chamber and is in thermal contact with the cold finger of the helium closed-cycle cryostat. The gold surface is not representative for interstellar grain surfaces, but it is an effective heat conductor, highly reflective in the mid-infrared, and chemically inert, *i.e.*, the substrate plays no role in catalyzing chemical reactions or processes at the substrate surface. Moreover, ice thicknesses are typically more than ten monolayers, reducing the role of the substrate. Therefore, it is well suited to study interstellar relevant reaction routes that occur on and in ice samples. The substrate temperature is varied between 12 and 300 K with a relative precision of 0.5 K through a cryogenic temperature controller (LakeShore model 340). To achieve temperatures as low as 12 K an aluminum thermal shield kept at ~77 K surrounds the cold finger and the back-side of the sample. The temperature of the sample is changed and monitored by means of heating wires and thermocouples, respectively. The heating wires are mounted

around the cold finger close to the substrate, while the two KP-type thermocouples are connected above and below the gold substrate. The absolute temperature accuracy is better than 2 K. This is checked by monitoring the well known desorption temperature of volatile species like for instance CO, N_2, and O_2 (Acharyya et al., 2007).

An all-metal high-vacuum stainless steel ice deposition dosing line is used to prepare, store and introduce gas mixtures into the main chamber. The pressure in the deposition dosing line is monitored mass independently by means of an active capacitance transmitter (Pfeiffer Vacuum, CMR361) in the range between 0.1 and 1100 mbar. Lower pressures are monitored with an active Pirani transmitter (Pfeiffer Vacuum, TPR280) ($5 \cdot 10^{-4} - 1000$ mbar). The deposition dosing line is first pre-pumped with a diaphragm pump (ABM, VDE 0530) and then with a 180 l/s (for N_2) turbomolecular pump (Pfeiffer Vacuum, TPH 180H) to reach low pressures ($< 5 \cdot 10^{-4}$ mbar). Gaseous species are admitted into the main chamber through a dosing line comprising of two separate all-metal leak valves connected to gas reservoirs. Therefore, different gasses can be prepared and stored in two different sections of the dosing line and then deposited separately or simultaneously onto the gold substrate. Deposition proceeds under an angle of 90° and 68°, respectively, and with a controllable flow between 10^{-8} and 10^{-7} mbar s^{-1}, where $1.3 \cdot 10^{-6}$ mbar s^{-1} corresponds to 1 Langmuir (L). Gas-phase species are monitored during deposition mass spectrometrically by means of the QMS, which is placed behind the substrate and mounted opposite to one of the two atom lines.

2.4.2 *Analytical Tools*

Ices are monitored *in situ* by means of RAIR spectroscopy using the FTIR, which covers the range between 4000 and 700 cm^{-1} ($2.5 - 14$ μm). A spectral resolution between 1 and 4 cm^{-1} is generally used and between 128 and 512 scans are co-added. The infrared beam coming from the FTIR is slowly diverging. Therefore, a series of $\lambda/4$ precision gold-coated mirrors (Edmund Optics and Thorlabs) is used to focus the beam onto the gold substrate (#5 in Fig. 2.2). The first one (M1) is a spherical mirror with a diameter of 76.2 mm and an effective focal length (EFL) of 762 mm. This mirror is used to gently converge the beam. The second (M2) and the fourth mirror (M4) are flat mirrors, while the third one (M3) is a spherical mirror with a diameter of 75.0 mm and an EFL of 500 mm. The latter focusses the beam onto the substrate with a glancing angle of $\sim 8°$. The main chamber mounts two Zinc Selenide (ZnSe) CF 35 view ports that act as a vacuum seal and allow the IR beam to enter and leave the chamber with a transmission $> 95\%$ in the range between $4 - 20$ μm. The out-going beam is then focussed into a narrow band and enters a liquid nitrogen cooled Mercury Cadmium Telluride (#7 in Fig. 2.2) detector by means of a 90° off-axis parabolic gold-coated mirror (M5) with a diameter of 50.8 mm and a reflected EFL of 50.8 mm. The external optics and the detector are mounted in metal boxes (#6 in Fig. 2.2). These boxes as well as the FTIR spectrometer are purged with dry-air to minimize atmospheric absorptions.

Two different experimental procedures are applied when using the FTIR. During pre-deposition experiments, ices are first deposited onto the gold substrate and subsequently exposed to atoms. To detect newly formed stable solid species, RAIR difference spectra (ΔAbsorbance) are acquired during atom exposure with respect to a background spectrum of the initial deposited ice. In co-deposition experiments, molecules and atoms are simultaneously deposited onto the substrate. The formation of intermediate species and final products is controlled by changing the deposited molecule/atom ratio. In this case, RAIR difference spectra are acquired during co-deposition with respect to a background spectrum of the bare gold substrate.

At the end of the atom exposure a TPD experiment can be performed: the sample is heated linearly (*i.e.*, with a constant rate between 0.1 and 10 K/min) till the ice is fully desorbed.

The thermal desorption can be followed spectroscopically by using the FTIR. Alternatively, the sample can be turned 135° to face the QMS. In this way, gas-phase species thermally desorbed from the ice are monitored mass spectrometrically. The desorbed species are recorded as a function of temperature by the QMS, which produces a signal proportional to the number of incoming molecules as a function of their mass to charge ratio (m/z). The incoming molecules first enter the ion source of the QMS, where they are ionized through electron bombardment by electrons released from a hot filament. The resulting ions are then focussed, selected and directed onto a Faraday detector, which collects the ions directly, allowing the ion current to be monitored. Alternatively, for higher sensitivity, a Channel Electron Multiplier (CEM) can be used. This type of detector is a Secondary Electron Multiplier (SEM) in which a large negative potential (~ - 2000 V) is used to attract the ions into the channel entrance. The channel is coated with a material that readily releases secondary electrons upon ion/electron impact. This produces a cascade of electrons down to the channel which can be detected, either as an electron current, or as a series of pulses.

TPD combined with a QMS is a sensitive technique, but it has several disadvantages: surface reaction products that remain in the solid phase cannot be probed *in situ*; additional surface reactions during the TPD (*i.e.*, during the linear heating of the ice and before complete desorption of the species) cannot be excluded; quantifying the desorbing species is not trivial as some of the interesting species have equal (*i.e.*, undistinguishable) masses and the analysis of the fractionated components of species upon electronic bombardment is not always straightforward. Finally, a TPD experiment inherently involves the destruction of the ice. Therefore, QMS data are mainly used here to constrain RAIR spectrocopy data acquired during atom exposure of the ice.

2.4.3 *Data Analysis*

After fitting the infrared spectra with connected straight baseline segments, the column densities (molecules cm^{-2}) of newly formed species can be determined from the integrated intensity of their infrared bands using a modified Lambert-Beer equation (Bennett et al., 2004):

$$N_X = \frac{\int A(\nu)d\nu}{S_X}, \tag{3}$$

where $A(\nu)$ is the integrated absorbance and S_X is the corresponding band strength. This equation can, however, only be used for thin ice layers. Teolis et al. (2007) showed that the proportionality between the optical depth and the ice abundance breaks down for thicker layers (~ 20 ML onwards); the integrated band area oscillates as a function of the layer thickness due to optical interference that is caused by the reflection at both the film-vacuum and film-substrate interfaces.

Since literature values of transmission band strengths cannot be used directly in reflectance measurements, an apparent absorption strength of stable species has to be calculated from calibration experiments. The determination of this apparent absorption strength is setup dependent. Therefore we performed a series of isothermal desorption experiments for the new apparatus introduced here to derive these values. Briefly, a layer of the selected ice is deposited at a temperature lower than its desorption temperature. The sample is then linearly heated to a temperature close to its desorption value. Infrared spectra are acquired regularly until the desorption of the ice is complete. The transition from zeroth-order to first-order desorption is assumed to occur at the onset to the submonolayer regime and appears in the desorption curve as a sudden change in slope (see Fig. 2.3). The apparent absorption strength

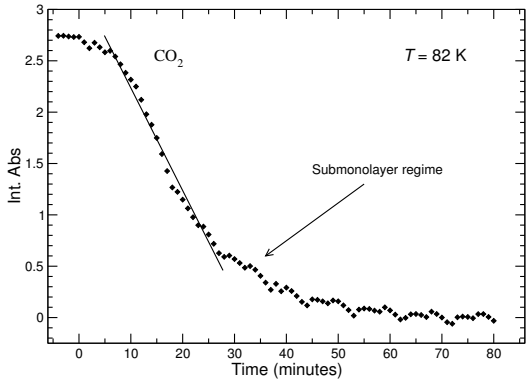

Figure 2.3: The decrease in integrated absorbance of CO_2 following desorption at a constant temperature of 82 K. The arrow indicates the transition point from the multi- to sub-monolayer regime.

in cm^{-1} ML^{-1} is then calculated by relating the observed integrated area to 1 ML in the modified Lambert-Beer equation. We estimate the uncertainty of band strengths determined in this way to be large but within 50% (also see Fuchs et al., 2009; Ioppolo et al., 2010; Fraser et al., 2001).

The determination of the band strength allows for a quantitative study of stable species formed upon atom exposure of the ice. This is mostly the case in pre-deposited experiments. Isothermal desorption experiments of unstable intermediate species cannot be performed and therefore their band strengths cannot be derived. Thus, a qualitative study is generally performed in co-deposition experiments where instable species are frozen in ice matrices and then detected in the infrared. In this case, formation trends of detected species are followed by integrating the corresponding band area as a function of time, *i.e.*, without calculating column densities. As a consequence, only formation trends of the same species obtained under different experimental conditions (*e.g.*, ice temperature, atom flux, ice composition) can be compared, but this still allows us to derive valuable information on the involved reaction network.

2.4.4 *Atom Beam Lines*

Two different atom sources are used, one (HABS) based on thermal cracking, and the other (MWAS) using a microwave discharge (#9 and #13 in Fig. 2.2). The two custom-made atom line chambers present identical geometrical characteristics (see Figs. 2.4 and 2.5): they are both pumped by 180 l/s (for N_2) turbomolecular pumps (Varian, TV 301 NAV); their room temperature base pressure is in the high 10^{-10} mbar regime (micro ion gauges, Granville-Phillips); they both are situated under an angle of 45° with respect to the substrate, both during single or simultaneous operation; a shutter is used to separate the lines from the main chamber; and a quartz pipe is placed after the shutter and along the path of the dissociated beam. The nose-shaped form of the pipe is designed to efficiently quench the excited electronic and rovibrational states of species through collisions with the walls of the pipe before they reach the ice sample. The geometry is designed in such a way that this is realized through at least four wall collisions of the atoms before leaving the pipe. In this way, “hot" species cannot reach the ice directly. In fact, throughout the calibration stage of the setup, several reactions have

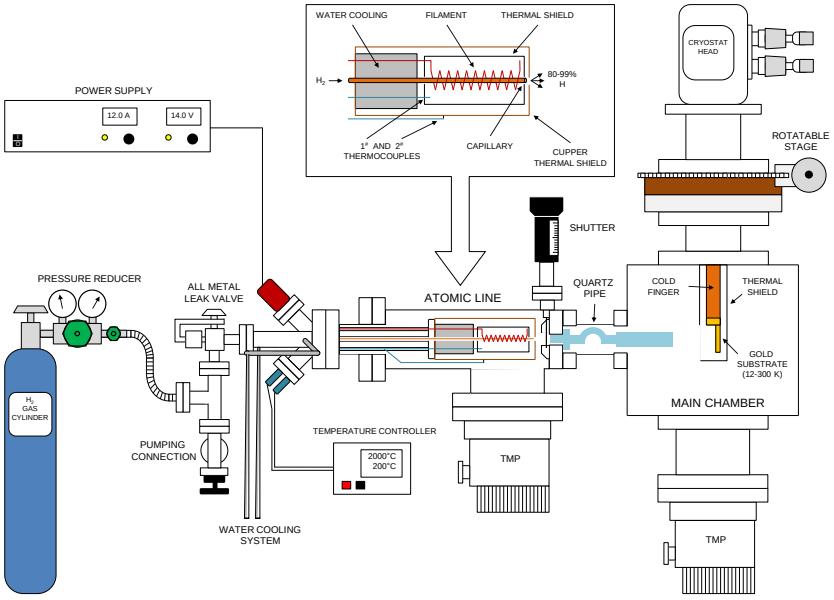

Figure 2.4: A schematic side-view of the atom line (HABS) with the thermal cracking H/D atom source and the main chamber.

been performed to probe the (non-)existence of excited states in the beamline. For example, the reaction $H_2 + O(^1D) \longrightarrow OH(^2\Pi) + H$ is exothermic and posesses no detectable temperature dependence in the gas-phase and is therefore assumed to proceed barrierless (Davidson et al., 1977). The reaction $H_2 + O(^3P) \longrightarrow OH + H$ on the other hand is endothermic and is therefore not expected to proceed. In a codeposition of H_2 and O on a cold surface, no large amount of potential products, OH or H_2O, can be found (Chapter 6). Therefore it is safe to assume that the fraction of $O(^1D)$ deposited on the surface is negligible or, alternatively, energy dissipation is fast enough to ensure that the excess energy cannot be used during reactions.

Two separate all-metal dosing lines are used to prepare and inlet pure gasses and mixtures into each of the atom sources (#10 and #14 in Fig. 2.2). The dosing lines are pre-pumped with the same diaphragm pump that is used for evacuating the deposition dosing line. Each of the atom lines is then pumped with a 70 l/s (for N_2) turbomolecular pump (Pfeiffer Vacuum, TMU 071P). The room temperature base pressure of these lines is $< 1 \cdot 10^{-5}$ mbar and is monitored by means of a compact process ion gauge for each line (Pfeiffer Vacuum, IMR 265).

2.4.4.1 *HABS*

An all-metal precision leak valve is used to admit H_2/D_2 molecules (99.8% purity, Praxair) from the all-metal dosing line into the capillary of a commercially-available and well-characterized thermal cracking source, a Hydrogen Atom Beam Source (HABS, Dr. Eberl MBE-Komponenten GmbH) (Tschersich & von Bonin, 1998; Tschersich, 2000; Tschersich et al., 2008), which is used to hydrogenate/deuterate the sample through heating the capillary from 300 to a maximum of 2250 K by a surrounding tungsten filament (see top-box in Fig. 2.4). During experiments the H + H_2 (D + D_2) flow through the capillary and the temperature of the tungsten filament are controlled and kept constant by adjusting the all-metal valve position and

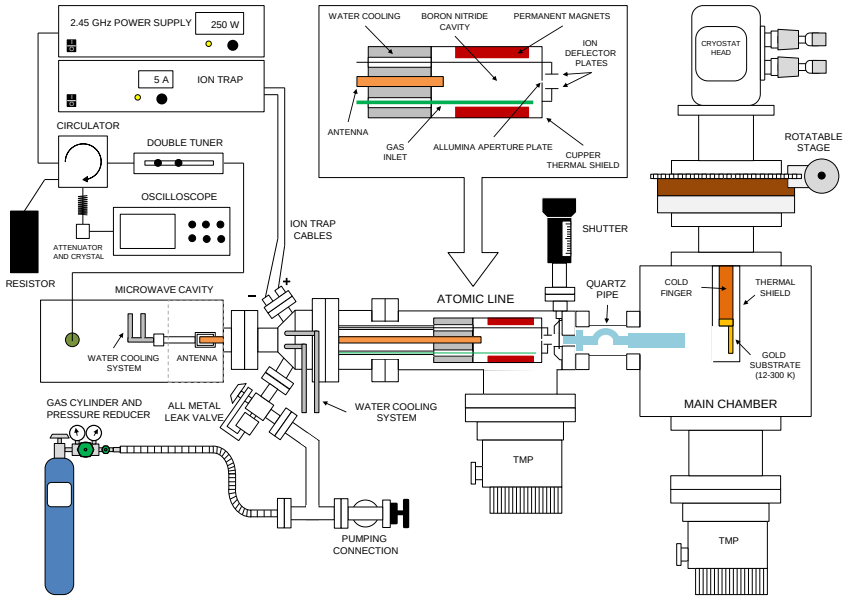

Figure 2.5: A schematic side-view of the atom line (MWAS) with the microwave plasma atom source and the main chamber.

the voltage of the power supply of the HABS (Delta Elektronika, SM 7020-D). The temperature of the filament is monitored by means of a C-type thermocouple placed close to the filament and inside the internal thermal shield. To prevent melting of components a water cooling system is implemented into the source, in thermal contact with an external copper thermal shield. The temperature of this shield is controlled with a second C-type thermocouple. The HABS is used in horizontal mode.

A wide range of atom-beam fluxes is accessible with this source by changing the pressure in the capillary pipe and/or the temperature of the filament. Typically values cover a range from 10^{11} to 10^{13} atoms cm^{-2} s^{-1}. Atom fluxes are measured at the sample position in the main chamber, following a procedure described in Section 2.4.5.1 (also see Bergh et al., 1999; Hidaka et al., 2007; Ioppolo et al., 2010).

As aforementioned, a quartz pipe is placed along the path of the beam (*i.e.*, after the shutter and before the sample in the main chamber) to cool the beam to room temperature. Previous experiments with liquid nitrogen cooled atom beams did not show any H/D-atom temperature dependence in CO hydrogenation reaction processes compared to experiments at room temperature (Watanabe & Kouchi, 2002). It is important to note that the relatively high temperature of 300 K of the incident H/D atoms in our experiments does not affect the experimental results, since H/D atoms are thermally adjusted to the surface temperature before they can react with other species through Langmuir-Hinshelwood mechanism, as shown in Fuchs et al. (2009); Hidaka et al. (2004); Watanabe et al. (2006).

2.4.4.2 *MWAS*

A Microwave Atom Source (MWAS, Oxford Scientific Ltd) is included in the second atom line to produce beams of different atoms and radicals (*e.g.*, H, D, O, OH, OD, N). Figure 2.5 shows

a schematic diagram of the MWAS. A 2.45 GHz microwave power supply (Sairem) produces up to 300 W that are coupled into a microwave cavity. Along this path a circulator is placed to avoid that the back-reflected power enters the power supply. A custom-made double tuner is placed after the circulator and before the microwave cavity to minimize the back-reflected power that ultimately is dissipated in a resistor. Part of the back-reflected signal is monitored by means of an oscilloscope (Tektronix, TDS 2012) connected to an attenuator and a crystal detector (Aertech Industries). An antenna (coaxial transmission line) connects the microwave cavity to a boron nitrite chamber in which gasses enter through the all-metal precision leak valve of the dosing line (see top-box in Fig. 2.5). A plasma is created in a coaxial waveguide by coupling a radially symmetric 2.45 GHz microwave field to ions on the 86 mT surface of a multi-polar magnetic array (permanent magnets). The plasma is enhanced by the electron cyclotron resonance (ECR) effect. A water cooling system keeps the source and particularly the antenna close to room temperature. Moreover, the absence of a hot filament permits operation with most gases including reactive gases such as oxygen and nitrogen.

A specially designed alumina aperture plate allows reactive neutrals to escape from the plasma. The addition of an ion-trap (*i.e.*, two metal plates charged by a Oxford Scientific DC power supplier) can deflect the residual ion content from the beam, preventing ion exposure of the sample. All the electronically and ro-vibrationally excited species coming from the source are quenched through multiple collisions on passing through a quartz pipe before they reach the sample. Different plasma cavity pressures and/or different plasma power values give access to a wide range of atom fluxes, typically between 10^{10} and 10^{13} atoms cm^{-2} s^{-1}. These numbers depend on the dissociated species (see next section).

2.4.5 *Beam Flux Determinations*

In order to measure the absolute D-atom fluxes for HABS and MWAS in the main chamber, the gold substrate is removed and the inlet of the QMS is placed at the center of the chamber facing the two atom lines, exactly at the same position and with the same angle that the substrate has when the ice is deposited and exposed to atom-beam bombardment (see also Ref. (Hidaka et al., 2007; Ioppolo et al., 2010)). Since the sensitivity of the standard $1 - 200$ amu QMS does not allow an accurate measurement at mass 1 amu, we measure the absolute D-atom fluxes instead of the H-atom fluxes for HABS and MWAS by following the aforementioned procedure. H-atom fluxes are then derived from the H/D ratio as obtained in selected experiments discussed in Section 2.4.5.1.

The other MWAS absolute atom fluxes (*e.g.*, oxygen and nitrogen) cannot be measured mass spectrometrically because the background signal from the fractionated molecular species coming from the molecular component of the beam and the residual gas in the main chamber interferes with the signal coming straight from the atom beam. Therefore, effective O/N-atom fluxes are derived at the ice surface by using a new calibration method described here for the first time and based on measuring the formation yield of final products of barrierless surface reactions (see Sections 2.4.5.2 and 2.4.5.3).

2.4.5.1 *H/D-atom beam fluxes*

The D-atom and D_2 molecule fluxes for both HABS and MWAS are measured by monitoring masses 2 and 4 amu, respectively. Once the source is turned on, an increase in intensity of the D atoms is monitored with the QMS. The QMS measurements do not directly give the D-atom

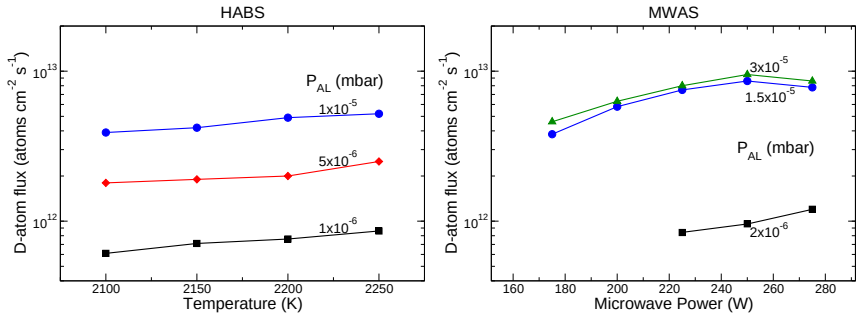

Figure 2.6: D-atom flux values as measured for the HABS (left panel) and the MWAS (right panel) at the substrate place for different parameter settings.

flux values. However, the increase in intensity of the QMS signal, ΔQ_D, is proportional to the increase in pressure in the main chamber, ΔP_D:

$$\Delta P_D = a \Delta Q_D. \tag{4}$$

The setup specific proportionality factor a is measured from eq. (4) by introducing in the main chamber D_2 molecules instead of D atoms. The choice of D_2 is given by the fact that the factor a is independent of gas species, because the density of molecules should be proportional to the density of produced ions in the QMS ion source. Furthermore, the D-atom beam contains a significant amount of undissociated D_2 molecules. Therefore, an exact measurement of ΔP_D is not trivial, while ΔP_{D_2} can be easily measured. The absolute D-atom fluxes are subsequently obtained from the following expression:

$$f_D = \frac{c_D \Delta P_D \langle v \rangle}{4 k_B T} = \frac{c_D a \Delta Q_D \langle v \rangle}{4 k_B T}, \tag{5}$$

where c_D is the calibration factor for the pressure gauge for D atoms taken from the specifications, $\langle v \rangle$ is the thermal velocity of the D atoms at 300 K, k_B is the Boltzmann constant, and T is the D-atom temperature. Different D-atom fluxes are obtained by varying the filament temperature and/or the D_2 inlet flow with the HABS, and by changing the plasma cavity pressure and/or plasma power with the MWAS. Figure 2.6 shows the D-atom flux values produced by the HABS (left panel) and by the MWAS (right panel), as measured at the substrate site for different parameter settings. The relative error for D-atom fluxes (HABS and MWAS) is within 10%. The absolute error is within 50%. These errors may seem large, but it should be noticed that here atom fluxes at the ice surface are actually determined experimentally, whereas in previous studies these numbers are generally only estimated.

Since an absolute H-atom flux cannot be directly measured, the comparison between H- and D-atom fluxes is difficult. We compared the H_2O_2 and D_2O_2 formation rate upon O_2 hydrogenation and deuteration, which is flux dependent, in two identical 25 K experiments for both the HABS and the MWAS. The H_2O_2 formation rate was found to be a factor of ~ 2 higher than the D_2O_2 formation rate for both sources. This value confirms our previous finding (Ioppolo et al., 2010) and is used here to scale H-atom fluxes with an uncertainty of 50%. This simplistic way of measuring a scaling factor between H- and D-atom fluxes does not however take into account that H and D atoms can differ by (*i*) sticking probability onto the surface, (*ii*) hopping rate, (*iii*) HO_2 + H (DO_2 + D) branching ratio and reaction barrier, (*iv*) desorption probability, and (*v*) recombination probability with other H/D atoms. Therefore, a new method for the determination of the H-atom fluxes, based on trapping H and D atoms

inside an O_2 ice matrix, is used by Fedoseev et al. (2015) In brief, the reaction H + O_2 → HO_2 is barrierless under certain incoming angles in the gas phase. During co-deposition experiments, the angle dependence has a negligible physical importance since the oxygen beam provides O_2 molecules with a range of different orientations at the surface before they can align (Chapter 4). Therefore, the amount of HO_2 (DO_2) formed in the ice is proportional to the H- (D)-atom flux, and gives us an estimate of the effective fluxes at the cold surface. Preliminary results show that the trends found in Fig. 2.6 for the D-atom fluxes are reproduced for the H-atom fluxes as well, but the ratio found for the effective H-versus-D flux is equal to one within the experimental uncertainties. Therefore, as mentioned above, the H-atom flux has an uncertainty of 50%.

2.4.5.2 *O-atom beam fluxes*

The effective MWAS O-atom fluxes (*i.e.*, oxygen atoms directly involved in surface reactions) are derived by measuring the final column density of newly formed ozone ice following co-deposition of ^{16}O atoms and $^{18}O_2$ molecules at 15 K. The reaction O_2 + O → O_3 is barrierless (Campbell & Gray, 1973; Lin & Leu, 1982), and therefore, we can safely assume that most of the oxygen atoms available for reaction on the surface will recombine to form ozone ice. Co-deposition experiments are used in order to avoid limitations in penetration depth of oxygen atoms into molecular oxygen ice.

Final fluxes are calculated from the knowledge of the duration of O-atom exposure, the number of monolayers of O_3 formed upon reaction, and assuming 1 ML = 10^{15} molecules cm^{-2}:

$$f_X = \frac{N_{X'} \cdot 10^{15}}{\text{exposure time}}, \tag{6}$$

where f_X is the O-atom flux, and $N_{X'}$ = N_{O_3} = $^{16}O^{18}O^{18}O$ + $^{16}O^{16}O^{16}O$ in monolayers. We do not count the $^{16}O_3$ contribution three times because solid $^{16}O_3$ is not likely to be formed through the sequential merging of ^{16}O atoms on the surface of the ice. Most of the $^{16}O_2$ can indeed form in the quartz pipe through recombination of ^{16}O atoms (see Section 2.4.4.2), or it originates from a not fully dissociated beam, mainly in the case that ^{16}O atoms form through dissociation of $^{16}O_2$ gas molecules. The overall contribution of $^{16}O_2$ originating from the atom line is considerably smaller when N_2O is used instead of $^{16}O_2$ as a precursor gas to produce ^{16}O atoms. This can be checked by comparing the amount of $^{16}O_3$ formed in the ice in co-deposition experiments of ^{16}O (from $^{16}O_2$) + $^{18}O_2$ at 15 K with the amount of $^{16}O_3$ formed in similar co-deposition experiments with ^{16}O from N_2O. Moreover, the amount of $^{16}O_3$ can be controlled by changing the ratio $^{16}O/^{18}O_2$. An over-abundance of $^{18}O_2$ minimizes the amount of $^{16}O_3$ formed in the ice because ^{16}O atoms react mostly with $^{18}O_2$. A negligible amount of $^{16}O_3$ in the co-deposition experiments gives $N_{O_3} \approx {}^{16}O^{18}O^{18}O$, and therefore a more direct and accurate O-atom flux value. This is true, especially when ^{16}O atoms are obtained from N_2O. Finally, the non-detection of the other ozone isotopologues (*e.g.*, $^{18}O^{16}O^{16}O$, $^{18}O^{16}O^{18}O$, or $^{18}O^{18}O^{18}O$) in our experiments indicates that isotopic exchange induced by surface destruction reactions, like O_3 + O → 2 O_2, is under the detection limit. Therefore, our method can be safely used to characterize the O-atom beam fluxes produced by the MWAS.

To quantify the amount of ozone produced in the oxygen flux-determination experiments, we derived the absorption band strength of ozone in two different ways: (i) performing an isothermal desorption experiment as described in Section 2.4.3 ; (ii) measuring the consumption of ozone through hydrogenation reactions and assuming that hydrogen can penetrate

Table 2.1: The effective O- and N-atom fluxes as derived from the formation yields of solid species in the ice upon barrierless reactions (see eq. 6).

Effective atom flux	High (at. cm^{-2} s^{-1})	Diss. ratio (%)	Low (at. cm^{-2} s^{-1})	Diss. ratio (%)
^{16}O from O_2	$9 \cdot 10^{11}$	8	$2 \cdot 10^{11}$	12
^{16}O from N_2O	$7 \cdot 10^{11}$	19	$1 \cdot 10^{11}$	10
^{15}N from $^{15}N_2$	$9 \cdot 10^{10}$	0.4	—	—
^{14}N from $^{14}N_2$	$8 \cdot 10^{10}$	0.4	—	—

only up to 2 ML of ozone ice. In the first case, in order to determine one monolayer of ozone, we first produce $^{16}O^{18}O^{18}O$ during 3 hrs of co-deposition of ^{16}O and $^{18}O_2$ at 35 K. Subsequently, an isothermal desorption experiment is performed at 58.5 K. From the offset between zeroth-order and first-order desorption we estimate the band strength of $^{16}O^{18}O^{18}O$. In the second case, a co-deposition of ^{16}O and $^{18}O_2$ at 15 K is performed for 3 hrs to form again $^{16}O^{18}O^{18}O$. The ice is then annealed to 50 K in order to remove the molecular oxygen and to realize a pure ozone ice. The $^{16}O^{18}O^{18}O$ ice is then exposed to H atoms at 15 K to monitor the destruction of the ozone layer. Assuming that only ~2 ML of ozone ice are fully hydrogenated (Romanzin et al., 2011), we derive the number of ozone molecules destroyed upon hydrogenation per monolayer, which gives us back the apparent band strength for $^{16}O^{18}O^{18}O$. The final band strength for ozone is confirmed within 30% of uncertainty by the two different methods.

The $^{16}O_3$ apparent band strength is obtained from the available data for $^{16}O^{18}O^{18}O$ for our setup and the ratio between the transmission band strengths for $^{16}O_3$ and $^{16}O^{18}O^{18}O$ (for the transmission band strength values see Sivaraman et al., 2011). According to eq. 6 standard O-atom fluxes span in the range between 10^{11} and 10^{12} atoms cm^{-2} s^{-1}. The O-atom flux values shown in Table 2.1 have to be considered as lower limits because (*i*) fluxes are derived indirectly (effective fluxes), (*ii*) some of the ^{16}O can recombine on the surface of the ice, and (*iii*) $^{16}O_2$ can potentially not be further oxygenated to form ozone because it is trapped into the $^{18}O_2$ matrix. The dissociation rates shown in Table 2.1 are obtained by comparing the undissociated molecular component of the beam (*i.e.*, N_2O, O_2, N_2) measured mass spectrometrically (*i.e.*, with the atom source on and the QMS placed at the center of the main chamber) with the O- and N-atom flux values as derived in Sections 2.4.5.2 and 2.4.5.3, respectively.

2.4.5.3 *N-atom beam fluxes*

As for the MWAS O-atom fluxes, the determination of effective nitrogen-atom fluxes is obtained indirectly by measuring the final column density of newly formed dinitrogen trioxide (N_2O_3) ice after co-deposition of ^{15}N atoms and NO molecules at 15 K. In this particular experiment, a sequence of barrierless (or very low barrier) surface reactions is involved in the formation of N_2O_3 (Campbell & Gray, 1973; Schieferstein et al., 1983; Markwalder et al., 1993): N + NO → N_2 + O, NO + O → NO_2, and NO_2 + NO → N_2O_3. Therefore in this specific case, N-atom fluxes are directly proportional to the amount of N_2O_3 formed in the ice, and are determined by using Eqn. 6, where f_X is the N-atom flux, and $N_{X'} = N_{N_2O_3}$ which is the amount of monolayers of N_2O_3 formed in the ice after a certain time of N-atom exposure.

As in Section 2.4.5.2, we use two different methods to obtain the apparent N_2O_3 band strength. In particular, two new co-deposition experiments of NO and O_2 are performed at 15 K. Also in this case N_2O_3 is formed through surface reactions. The ice obtained from these two experiments is in both cases heated up to remove the NO trapped in the ice. In one of the two experiments, the ice temperature is then kept at 121 K to monitor the desorption of N_2O_3 (isothermal desorption experiment). From this experiment we obtain the band strength for N_2O_3, as discussed in the latter sections. In the second experiment, the ice is cooled down again to 15 K and subsequently hydrogenated to see the destruction of N_2O_3. The penetration depth of hydrogen into N_2O_3 ice is expected to involve only a few monolayers, as for O_3, CO, and NO ice (Romanzin et al., 2011; Fuchs et al., 2009; Fedoseev et al., 2012). Therefore, assuming that only ~2 ML of N_2O_3 are consumed by the surface hydrogenation of the ice, we can estimate the band strength of N_2O_3 which is found to be consistent with the value obtained from the isothermal desorption experiment within 40% of uncertainty.

The N-atom flux values are roughly one order of magnitude lower than the O-atom values (see Table 2.1). As explained in Section 2.4.5.2, these values are all lower limits, because of the way the fluxes are derived. In the specific case of nitrogen fluxes, the formation of N_2O_3 is a three step reaction, and therefore the single reactant can further react with the others to form N_2O_3, or alternatively desorb, or be trapped in a NO matrix. Therefore, we expect the O- and N-atom absolute fluxes to be higher than reported in Table 2.1.

BIBLIOGRAPHY

Abdulgalil, A. G. M., Marchione, D., Thrower, J. D., et al. 2013, Royal Society of London Philosophical Transactions Series A, 371, 10586

Acharyya, K., Fuchs, G. W., Fraser, H. J., van Dishoeck, E. F., & Linnartz, H. 2007, Astron. Astrophys., 466, 1005

Allodi, M. A., Ioppolo, S., Kelley, M. J., McGuire, B. A., & Blake, G. A. 2014, Phys. Chem. Chem. Phys., 16, 3442

Anton, R., Wiegner, T., Naumann, W., et al. 2000, Review of Scientific Instruments, 71

Baouche, S., Gamborg, G., Petrunin, V. V., et al. 2006, J. Chem. Phys., 125, 4712

Baratta, G. A., Leto, G., & Palumbo, M. E. 2002, Astron. Astrophys., 384, 343

Bennett, C. J., Ennis, C. P., & Kaiser, R. I. 2014, Astrophys. J., 782, 63

Bennett, C. J., Jamieson, C., Mebel, A. M., & Kaiser, R. I. 2004, Phys. Chem. Chem. Phys., 6, 735

Bergh, H. S., Gergen, B., Nienhaus, H., et al. 1999, Rev. Sci. Instrum., 70, 2087

Bernstein, M. P., Dworkin, J. P., Sandford, S. A., Cooper, G. W., & Allamandola, L. J. 2002, Nature, 416, 401

Bertin, M., Fayolle, E. C., Romanzin, C., et al. 2012, Phys. Chem. Chem. Phys., 14, 9929

Bolina, A. S., Wolff, A. J., & Brown, W. A. 2005, J. Phys. Chem. B, 109, 16836

Bossa, J.-B., Isokoski, K., de Valois, M. S., & Linnartz, H. 2012, Astron. Astrophys., 545, A82

Brown, W. A., Viti, S., Wolff, A. J., & Bolina, A. S. 2006, Faraday Discuss., 133, 113

Campbell, I. M. & Gray, C. N. 1973, Chem. Phys. Lett., 18, 607

Chen, Y.-J., Chuang, K.-J., Muñoz Caro, G. M., et al. 2014, Astrophys. J., 781, 15

Davidson, J. A., Schiff, H. I., Streit, G. E., et al. 1977, J. Chem. Phys., 67, 5021

Dulieu, F., Congiu, E., Noble, J., et al. 2013, Scientific Reports, 3, 1338

Duvernay, F., Dufauret, V., Danger, G., et al. 2010, Astron. Astrophys., 523, A79

Ehrenfreund, P., Boogert, A. C. A., Gerakines, P. A., Tielens, A. G. G. M., & van Dishoeck, E. F. 1997, Astron. Astrophys., 328, 649

Ehrenfreund, P., Dartois, E., Demyk, K., & D'Hendecourt, L. 1998, Astron. Astrophys., 339, L17

Fayolle, E. C., Bertin, M., Romanzin, C., et al. 2011, Astrophys. J. Lett., 739, L36

Fedoseev, G., Ioppolo, S., Lamberts, T., et al. 2012, J. Chem. Phys., 137, 054714

Fedoseev, G., Ioppolo, S., & Linnartz, H. 2015, Monthly Notices of the Royal Astronomical Society, 446, 449

Fletcher, N. H. 1971, Reports on Progress in Physics, 34, 913

Fraser, H. J., Collings, M. P., McCoustra, M. R. S., & Williams, D. A. 2001, Mon. Not. R. Astron. Soc., 327, 1165

Fuchs, G. W., Cuppen, H. M., Ioppolo, S., et al. 2009, Astron. Astrophys., 505, 629

Fulvio, D., Sivaraman, B., Baratta, G. A., Palumbo, M. E., & Mason, N. J. 2009, Spectrochimica Acta Part A: Molecular Spectroscopy, 72, 1007

Gavilan, L., Vidali, G., Lemaire, J. L., et al. 2012, Astrophys. J., 760, 35

Gerakines, P. A., Schutte, W. A., Greenberg, J. M., & van Dishoeck, E. F. 1995, Astron. Astrophys., 296, 810

Gibb, E. L., Whittet, D. C. B., & Schutte et al, W. A. 2000, Astrophys. J., 536, 347

Green, S. D., Bolina, A. S., Chen, R., et al. 2009, Mon. Not. R. Astron. Soc., 398, 357

Gudipati, M. S. & Yang, R. 2012, The Astrophysical Journal Letters, 756, L24

Hagen, W., Allamandola, L. J., & Greenberg, J. M. 1979, Astrophys. & Space Sci., 65, 215

Hagen, W., Tielens, A. G. G. M., & Greenberg, J. M. 1983, Astron. Astrophys. Suppl., 51, 389

He, J., Jing, D., & Vidali, G. 2014, Phys. Chem. Chem. Phys., 16, 3493

Hidaka, H., Kouchi, A., & Watanabe, N. 2007, J. Chem. Phys., 126, 204707

Hidaka, H., Watanabe, N., Shiraki, T., Nagaoka, A., & Kouchi, A. 2004, Astrophys. J., 614, 1124

Hiraoka, K., Ohashi, N., Kihara, Y., et al. 1994, Chem. Phys. Lett., 229, 408

Hony, S. 2003, PhD thesis, University of Amsterdam

Ioppolo, S., Cuppen, H. M., Romanzin, C., van Dishoeck, E. F., & Linnartz, H. 2008, Astrophys. J., 686, 1474
Ioppolo, S., Cuppen, H. M., Romanzin, C., van Dishoeck, E. F., & Linnartz, H. 2010, Phys. Chem. Chem. Phys., 12, 12065
Islam, F., Baratta, G. A., & Palumbo, M. E. 2014, Astron. Astrophys., 561, A73
Jones, B. M. & Kaiser, R. I. 2013, The Journal of Physical Chemistry Letters, 4, 1965
Kaiser, R. I., Maity, S., & Jones, B. M. 2014, Phys. Chem. Chem. Phys., 16, 3399
Karssemeijer, L. J., Ioppolo, S., van Hemert, M. C., et al. 2014, Astrophys. J., 781, 16
Lin, C. L. & Leu, M. T. 1982, Int. J. Chem. Kinet., 14, 417
Loeffler, M. J. & Baragiola, R. A. 2010, The Journal of Chemical Physics, 133,
Loeffler, M. J., Baratta, G. A., Palumbo, M. E., Strazzulla, G., & Baragiola, R. A. 2005, Astron. Astrophys., 435, 587
Markwalder, B., Gozel, P., & van den Bergh, H. 1993, J. Chem. Phys., 97, 5260
McCullough, R. W., Geddes, J., Donnelly, A., et al. 1993, Meas. Sci. Technol., 4, 79
Minissale, M., Fedoseev, G., Congiu, E., et al. 2014, Phys. Chem. Chem. Phys., 16, 8257
Mispelaer, F., Theulé, P., Aouididi, H., et al. 2013, Astron. Astrophys., 555, A13
Muñoz Caro, G. M., Meierhenrich, U. J., Schutte, W. A., et al. 2002, Nature, 416, 403
Nagaoka, A., Watanabe, N., & Kouchi, A. 2007, The Journal of Physical Chemistry A, 111, 3016
Noble, J. A., Dulieu, F., Congiu, E., & Fraser, H. J. 2011, Astrophys. J., 735, 121
Oba, Y., Watanabe, N., Kouchi, A., Hama, T., & Pirronello, V. 2010, Astrophys. J. Lett., 712, L174
Öberg, K. I., Fayolle, E. C., Cuppen, H. M., van Dishoeck, E. F., & Linnartz, H. 2009, Astron. Astrophys., 505, 183
Öberg, K. I., van Broekhuizen, F., Fraser, H. J., et al. 2005, ApJ Suppl., 621, L33
Paardekooper, D. M., Bossa, J.-B., Isokoski, K., & Linnartz, H. 2014, Review of Scientific Instruments, 85,
Palumbo, E. M., Baratta, G. A., Collings, M. P., & McCoustra, M. R. S. 2006, Phys. Chem. Chem. Phys., 8, 279
Palumbo, M., Baratta, G., Leto, G., & Strazzulla, G. 2010, Journal of Molecular Structure, 972, 64 , horizons in hydrogen bond research 2009 A Collection of Papers from the {XVIIIth} International Conference "Horizons in Hydrogen Bond Research", Paris, France, 14âĂŞ18 September 2009
Palumbo, M. E. & Strazzulla, G. 1993, Astron. Astrophys., 269, 568
Pirronello, V., Biham, O., Liu, C., Shen, L., & Vidali, G. 1997, Astrophys. J. Lett., 483, L131
Raut, U. & Baragiola, R. A. 2011, Astrophys. J. Lett., 737, L14
Raut, U. & Baragiola, R. A. 2013, Astrophys. J., 772, 53
Raut, U., Fulvio, D., Loeffler, M. J., & Baragiola, R. A. 2012, Astrophys. J., 752, 159
Romanzin, C., Ioppolo, S., Cuppen, H. M., van Dishoeck, E. F., & Linnartz, H. 2011, J. Chem. Phys., 134, 084504
Sabri, T., Gavilan, L., Jäger, C., et al. 2014, Astrophys. J., 780, 180
Sandford, S. A. & Allamandola, L. J. 1988, Icarus, 76, 201
Schieferstein, M., Kohse-Höinghaus, K., & Stuhl, F. 1983, Ber. Bunsenges. Phys. Chem., 87, 361
Sibener, S. J., Buss, R. J., Ng, C. Y., & Lee, Y. T. 1980, Review of Scientific Instruments, 51
Sivaraman, B., Mebel, A. M., Mason, N. J., Babikov, D., & Kaiser, R. I. 2011, Phys. Chem. Chem. Phys. (Incorporating Faraday Transactions), 13, 421
Sivaraman, B., Raja Sekhar, B. N., Fulvio, D., et al. 2013, J. Chem. Phys., 139, 074706
Stevenson, K. P., Kimmel, G. A., DohnÃąlek, Z., Smith, R. S., & Kay, B. D. 1999, Science, 283, 1505
Teolis, B. D., Loeffler, M. J., Raut, U., Famá, M., & Baragiola, R. A. 2007, Icarus, 190, 274
Thrower, J., Nilsson, L., Jørgensen, B., et al. 2011, European Astronomical Society Publications Series, 46, 453
Tielens, A. G. G. M. 2013, Reviews of Modern Physics, 85, 1021
Timmermans, E., Jonkers, J., Thomas, I., et al. 1998, Spectrochimica Acta Part B: Atomic Spectroscopy, 53, 1553
Tschersich, K. G. 2000, J. Appl. Phys., 87, 2565

Tschersich, K. G., Fleischhauer, J. P., & Schuler, H. 2008, J. Appl. Phys., 104, 034908

Tschersich, K. G. & von Bonin, V. 1998, J. Appl. Phys., 84, 4065

Watanabe, N., Hidaka, H., & Kouchi, A. 2006, in AIP Conf. Ser., Vol. 855, Astrochemistry - From Laboratory Studies to Astronomical Observations, ed. R. I. Kaiser, P. Bernath, Y. Osamura, S. Petrie, & A. M. Mebel, 122–127

Watanabe, N., Kimura, Y., Kouchi, A., et al. 2010, Astrophys. J. Lett., 714, L233

Watanabe, N. & Kouchi, A. 2002, Astrophys. J. Lett., 571, L173